International Journal of Scientific Research and Modern Technology (IJSRMT) ijsrmt.com
Volume 5, Issue 11, 2026
DOI: https://doi.org/10.38124/ijsrmt.v5i11.1805

Design and Fabrication of a Low-Cost Broadband Induction-Coil Magnetometer with Synchronized Data Acquisition for Magnetotelluric Groundwater Exploration

E. O. Ogunniyi[1]; A. O. Ademoroti[2]; O. V. Enuiyin[3]; T. Jombo[4]; A. O. Ogunbiyi[5]

[1,2,3,5]Department of Physics, Bamidele Olumilua University of Education, Science and Technology, Ikere-Ekiti, Ekiti State, Nigeria
[4]Department of Physics and Electronics, Adekunle Ajasin University, Akungba-Akoko, Ondo State, Nigeria

Publication Date: 2026/11/23

Abstract

Magnetotelluric (MT) and Audio-Frequency Magnetotelluric (AMT) methods are vital non-invasive geophysical techniques for deep aquifer characterization. However, commercial MT instrumentation remains prohibitively expensive, limiting extensive hydrogeological surveys in resource-constrained regions. This paper presents the engineering design, component-level fabrication, laboratory calibration, and field validation of a low-cost, high-sensitivity broadband Induction-Coil Magnetometer (ICM) integrated with a high-resolution, GNSS-synchronized Data Acquisition (DAQ) system. The magnetic sensor incorporates a high-permeability Metglas 2605SA1 amorphous alloy laminated core (0.8 m length, 25 mm diameter) wound with 35,000 turns of segmented AWG 32 enamelled copper wire across ten bobbins and enclosed within a slotted electrostatic Faraday shield. The Analog Front-End (AFE) features an ultra-low-noise bipolar operational amplifier (OPA211, 1.1 nV/$\sqrt{Hz}$) paired with an active bandpass filter (0.001 Hz – 10 kHz). Digitization is accomplished using a 24-bit Delta-Sigma (ΔΣ) analog-to-digital converter (ADS1256) interfaced via galvanic isolation to an ARM Cortex-M4 microcontroller (STM32F407) and a GNSS module (u-blox NEO-M8N) providing sub-microsecond 1 Pulse-Per-Second (1PPS) time-stamping for remote-reference processing. Calibration inside a triple-layer Mu-Metal chamber demonstrates a corner frequency of 10 Hz, a flat passband sensitivity of 2.42 V / nT from 10 Hz to 5 kHz, and an equivalent magnetic noise floor of 8.2 fT/$\sqrt{Hz}$ (0.0082 pT$\sqrt{Hz}$) at 1 k Hz. Co-located field deployment in the fractured crystalline basement of Akungba-Akoko, Southwestern Nigeria, benchmarked against a commercial receiver (Metronix ADU-07e), yielded an impedance tensor cross-coherence $R^2 > 0.94$ and delineated a deep fractured aquifer between 120 m and 220 m depth within a 4.2 % margin of regional borehole logs. Fabricated at a total unit cost of $616.90, this open-hardware system provides an accessible, field-ready platform for regional hydrogeological and geophysical exploration.

Keywords: *Magnetotellurics (MT); Induction-Coil Magnetometer; Broadband Signal Conditioning; GNSS Synchronization; 24-bit Data Acquisition; Groundwater Exploration.*

I. INTRODUCTION

Groundwater scarcity represents a critical socioeconomic and public health challenge in arid and developing regions, necessitating robust, non-invasive geophysical techniques to delineate deep aquifer structures, fault zones, and basement topographies (Auken et al., 2009; Sendrós et al., 2020). Among electromagnetic (EM) methods, Audio-Frequency Magnetotellurics (AMT) and broadband Magnetotellurics (MT) utilize naturally occurring transient EM fields to image subsurface electrical resistivity contrasts across depths ranging from tens of meters to tens of kilometers (Cagniard, 1953; Vozoff, 1991; Simpson & Bahr, 2005; Chave & Jones, 2012). High-frequency natural signals (> 1 Hz) originate primarily from global lightning activity

Ogunniyi, E. O., Ademoroti, A. O., Enuiyin, O. V., Jombo, T., & Ogunbiyi, A. O. (2026). Design and Fabrication of a Low-Cost Broadband Induction-Coil Magnetometer with Synchronized Data Acquisition for Magnetotelluric Groundwater Exploration. *International Journal of Scientific Research and Modern Technology*, *5*(11), 1–14. https://doi.org/10.38124/ijsrmt.v5i11.1805

within the Earth–ionosphere waveguide (Schumann resonances), whereas low-frequency signals (1 Hz) stem from solar wind interactions with the Earth's magnetosphere (Ward & Hohmann, 1988; Garcia & Jones, 2002).

Because water-bearing fractures and weathered regolith display significant electrical conductivity contrasts relative to surrounding unweathered crystalline basement rocks, MT and AMT methods offer exceptional utility for hydrogeological mapping (Christensen et al., 2006; Kirsch, 2009; Spichak & Manzella, 2009). Accurately measuring dynamic natural magnetic field variations (Hx, Hy Hz) requires sensors with sub-picotesla noise floors across wide operational bandwidths (Tumanski, 2007; Korepanov & Pronenko, 2010; Coppo et al., 2015). While fluxgate magnetometers are effective for DC and ultra-low-frequency geomagnetic monitoring (< 1 Hz), they lack the high-frequency sensitivity required for shallow-to-intermediate groundwater targets (10 Hz – 10 k Hz) (Ripka, 2001; Ripka & Janosek, 2010; Grosz & Paperno, 2012). Conversely, commercial Induction-Coil Magnetometers (ICMs) and multi-channel MT receivers cost tens of thousands of dollars per station, creating severe financial barriers for academic research and regional groundwater surveys in developing nations (Junge, 1996; Unsworth, 2007; Edel et al., 2014).

Furthermore, reliable MT impedance estimation depends heavily on remote-reference cross-coherence processing to suppress localized cultural and anthropogenic electromagnetic noise (Gamble et al., 1979; Egbert, 1997; Yang & Oldenburg, 2012). Remote-reference processing requires sub-microsecond time synchronization across spatially separated recording stations (Nichols et al., 1988; Zonge & Hughes, 1991). Recent advancements in low-cost 32-bit microcontrollers, ultra-low-noise operational amplifiers, and 24-bit Delta-Sigma (ΔΣ) Analog-to-Digital Converters (ADCs) provide a viable pathway toward custom, open-hardware geophysical instrumentation capable of rivaling commercial systems (Ferguson, 2012; Macnae & Yang, 2015; Carbone et al., 2017).

This paper presents the complete engineering design, component-level fabrication, laboratory calibration, and field validation of a low-cost broadband Induction-Coil Magnetometer integrated with a GNSS-synchronized 24-bit DAQ system. Fabricated at a total unit cost of $616.90, the system's spectral noise floor, transfer function, and subsurface imaging accuracy are benchmarked directly against commercial MT instrumentation in a hydrogeologically complex fractured crystalline basement terrain.

II. GEOLOGICAL AND HYDROGEOLOGICAL SETTING

Field validation was conducted in Akungba-Akoko, Akoko South-West Local Government Area, Ondo State, Southwestern Nigeria (Figure 1). Geologically, the study area lies within the Precambrian Basement Complex of Southwestern Nigeria, dominated by migmatite-gneiss complexes, porphyritic granite intrusions, and quartzite ridges (Rahaman, 1988; Olayinka & Barker, 1990).

To evaluate instrument resilience against varying levels of cultural electromagnetic interference, an 800 m survey transect was established across three distinct land-use zones along the fractured basement transition corridor:

- *Adekunle Ajasin University (AAUA) Main Campus Sector:*

  Located directly off the Ikare–Akungba highway, characterized by moderate institutional electrical activity and shallow regolith cover.

- *Boys Hostel Residential Axis:*

  Extending north-northeast from the AAUA Main Gate along the Ikare–Akungba corridor, representing a high-density residential zone with elevated 50 Hz power-line harmonics.

- *Akungba–Iwaro Oka-Akoko Corridor:*

  Extending east-southeast toward the hilly terrain of Oka-Akoko, characterized by outcropping granite gneisses and deep structural lineaments.

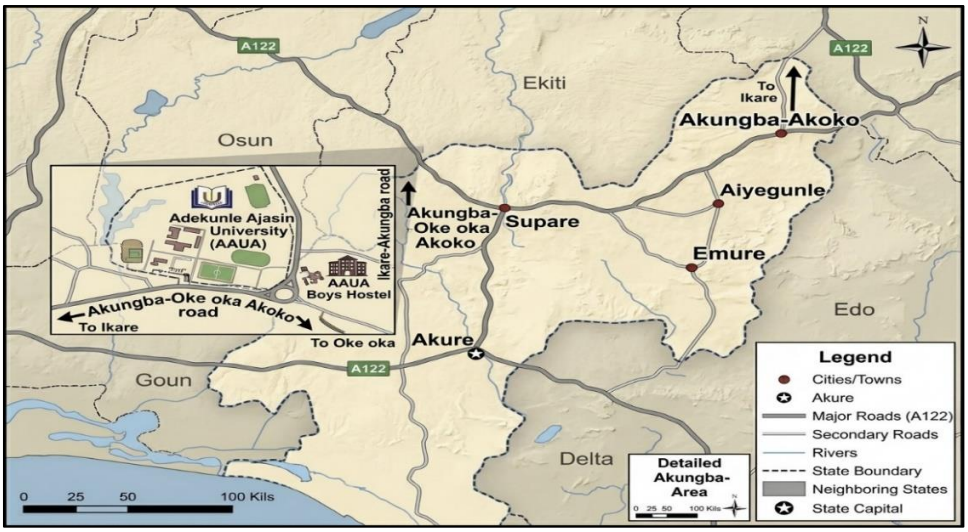


Fig 1 Regional Geological and Location Map of the Study Area in Akungba-Akoko, Ondo State, Nigeria, Illustrating the 800 m MT Survey Transect Across the Fractured Precambrian Basement Transition Zone.

Hydrogeologically, unweathered crystalline basement rocks exhibit negligible primary porosity and permeability. Groundwater occurrence and storage in this terrain are strictly controlled by secondary porosity developed within the weathered overburden (regolith) and deep fractured bedrock zones (Satpathy & Kanungo, 1976; Olorunfemi & Faseyi, 1993). Delineating the depth, thickness, and lateral continuity of low-resistivity water-saturated fracture zones (20 – 50 Ωm) beneath resistive weathered and fresh granite (> 600 Ωm}) requires broadband electromagnetic sounding capable of resolving subsurface structures from 10 m down to 300 m depth.

III. SYSTEM ARCHITECTURE AND HARDWARE DESIGN

The complete instrument architecture comprises three modular sub-assemblies: (1) the Magnetic Core and Segmented Induction-Coil Sensor, (2) the Analog Front-End (AFE) Signal Conditioning Circuit, and (3) the GNSS-Synchronized 24-bit Digitization and Storage Unit (Figure 2).

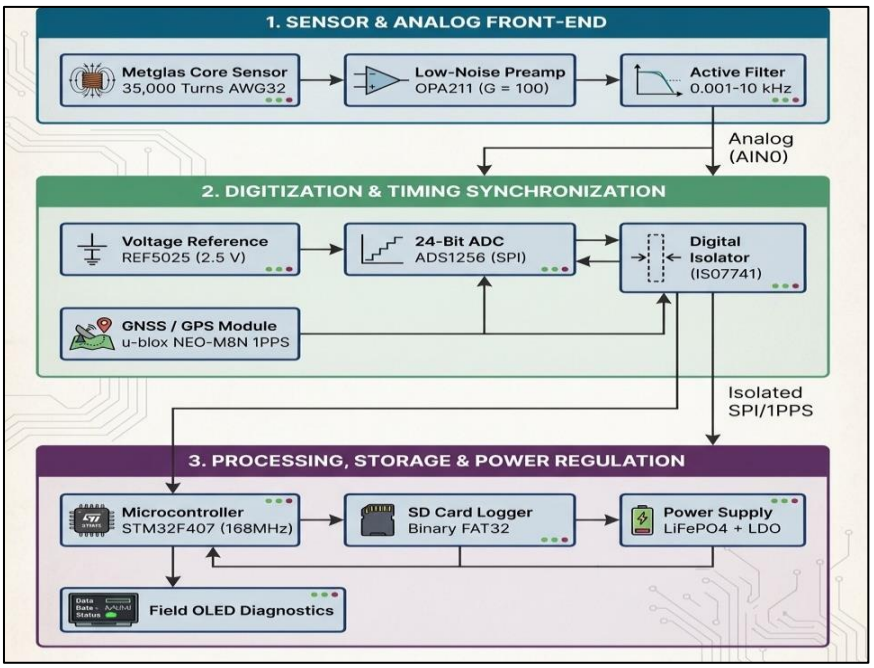


Fig 2 Functional Block Diagram of the Broadband Induction-Coil Magnetometer and GNSS-synchronized 24-bit Magnetotelluric Data Acquisition System.

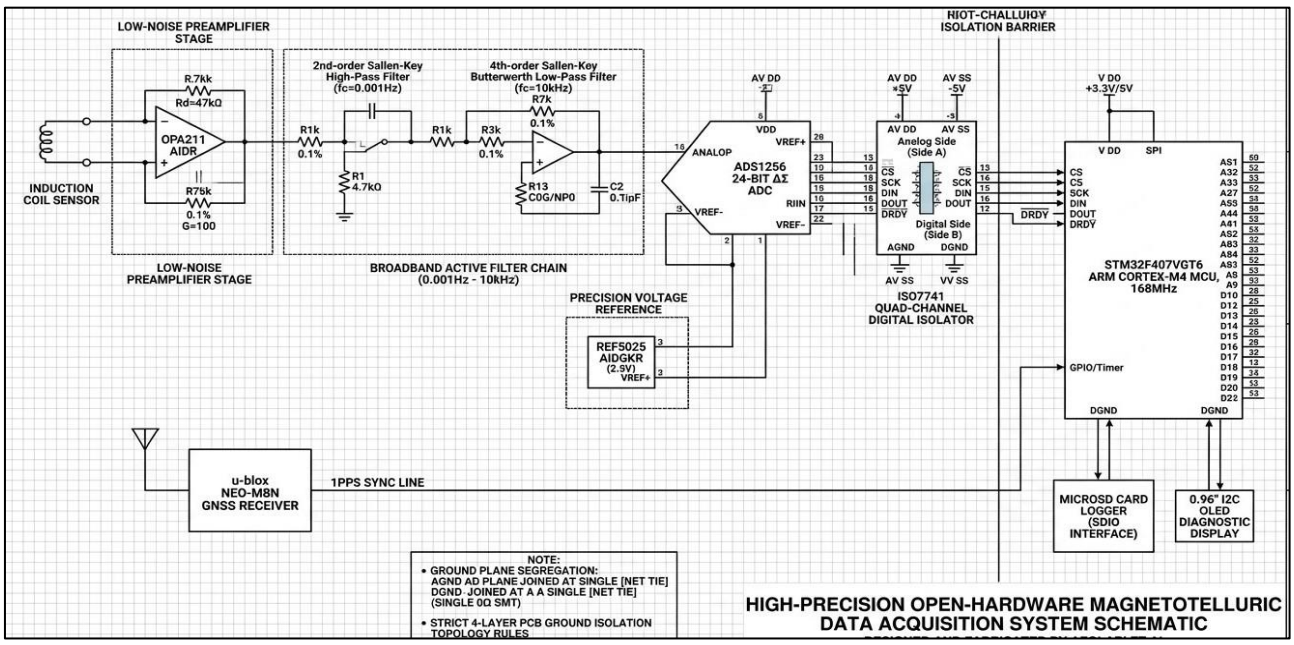


Fig 3 Complete Mixed-Signal Circuit Schematic of the Magnetotelluric Data Acquisition System, Illustrating the OPA211 Ultra-Low-Noise Differential Preamplifier, Sallen-Key Active Bandpass Filter Stages, REF5025 2.5 V Precision Reference, ADS1256 24-bit ΔΣ ADC, ISO7741 Galvanic Isolation Barrier, STM32F407VGT6 ARM Cortex-M4 Microcontroller, and u-blox NEO-M8N 1PPS GNSS Timing Interface.

➢ *Theoretical Sensor Physics and Coil Fabrication*

An induction-coil magnetometer operates in accordance with Faraday's Law of Electromagnetic Induction. A time-varying external geomagnetic flux density B(t) induces an electromotive force (EMF), e(t), across the coil windings given by:

$$e(t) = -N \cdot A \cdot \mu_{eff} \cdot \frac{dB(t)}{dt}$$

Where N=35,000 is the total number of wires turns, A = 4.91 x 10^{-4} m2 is the core cross-sectional area (radius r = 12.5mm), and μ_{eff} is the effective relative magnetic permeability of the core.

To maximize sensitivity while minimizing core weight, a high-permeability amorphous alloy ribbon stack (Metglas 2605SA1, bulk relative permeability μr ≈ 45,000) of length L=800mm was utilized. The effective permeability μ_{eff} is governed by the core demagnetization factor N_d:

$$\mu_{eff} = \frac{\mu_r}{1+N_d(\mu_r-1)}$$

For a cylindrical rod with length-to-diameter ratio m = L/D = 800/25 = 32, the empirical demagnetization factor N_d is given by Bozorth (1951):

$$N_d \approx \frac{ln(2m)-1}{m^2} \approx \frac{ln(64)-1}{1024} \approx 0.00308$$

Substituting μr = 45,000 and N_d = 0.00308 yields an effective core permeability of $\mu_{eff} \approx 322$Inter-winding parasitic capacitance Cp lowers the sensor's self-resonant frequency $f_r = \frac{1}{(2\pi\sqrt{LC_p})}$ which can restrict the upper operational bandwidth (Webb & Constable, 1989; Korepanov & Pronenko, 2010). To minimize Cp, the 35,000-turn winding was distributed evenly across 10 segmented, 3D-printed nylon bobbins (3,500 turns per section) connected in series using AWG 32 (0.20 mm diameter) polyurethane-enamelled copper wire. An electrostatic Faraday shield fabricated from 0.05 mm high-purity copper foil was wrapped around the winding assembly with an unclosed 3 mm longitudinal gap; this eliminates capacitive electric-field coupling while preventing shorted-turn eddy current attenuation. The entire sensor assembly was encapsulated in low-viscosity hydrophobic epoxy resin inside a non-magnetic, waterproof PVC pressure housing (900 mm x 90 mm).

➢ *Analog Front-End (AFE) Signal Conditioning*

The differential output of the induction coil is coupled directly to a low-noise instrumentation preamplifier built around the OPA211 bipolar operational amplifier, selected for its ultra-low broadband voltage noise density ($1.1nV/\sqrt{Hz}$ at 1 kHz) and low 1/f noise corner (1 Hz). A precision damping resistor ($R_d = 47k\Omega$) connected across the coil terminals enforces critical damping (Q = 0.707), flattening the resonant peak into a uniform passband response (Macnae & Yang, 2015).

The signal conditioning chain consists of three cascaded stages utilizing OPA4192 precision operational amplifiers:

- *Low-Noise Preamplifier Stage:*

Configured for a fixed differential voltage gain Gain G_1=100V/V (40dB).

- *Active High-Pass Filter (HPF):*

A 2nd-order Sallen-Key high-pass filter ($f_c = 0.001Hz$) to reject DC thermal offsets and ultra-long-period geomagnetic drift.

- *Active Anti-Aliasing Low-Pass Filter (LPF):*

A 4th-order Sallen-Key Butterworth low-pass filter ($f_c = 10kHz$) constructed with temperature-stable C0G/NP0 ceramic capacitors (1 % tolerance) and 0.1% thin-film metal resistors to ensure linear phase response across the passband.

➢ *GNSS-Synchronized Data Acquisition and Firmware Architecture*

Analog-to-digital conversion is executed by an ADS1256 24-bit Delta-Sigma (ΔΣ) ADC driven by a precision, ultra-low-noise 2.5 V voltage reference (REF5025, temperature drift ≤ 3 ppm / °C). To prevent digital switching noise from contaminating the analog front-end, the ADC communicates with an STM32F407VGT6 32-bit ARM Cortex-M4 microcontroller (168 M Hz) across an isolated Serial Peripheral Interface (SPI) bus utilizing an ISO7741 quad-channel digital isolator.Inter-station timing synchronization required for remote-reference MT processing is achieved by routing the 1 Pulse-Per-Second (1PPS) timing output of an onboard u-blox NEO-M8N GNSS receiver directly into a dedicated hardware timer capture interrupt on the STM32F407 microcontroller (Figure 4).

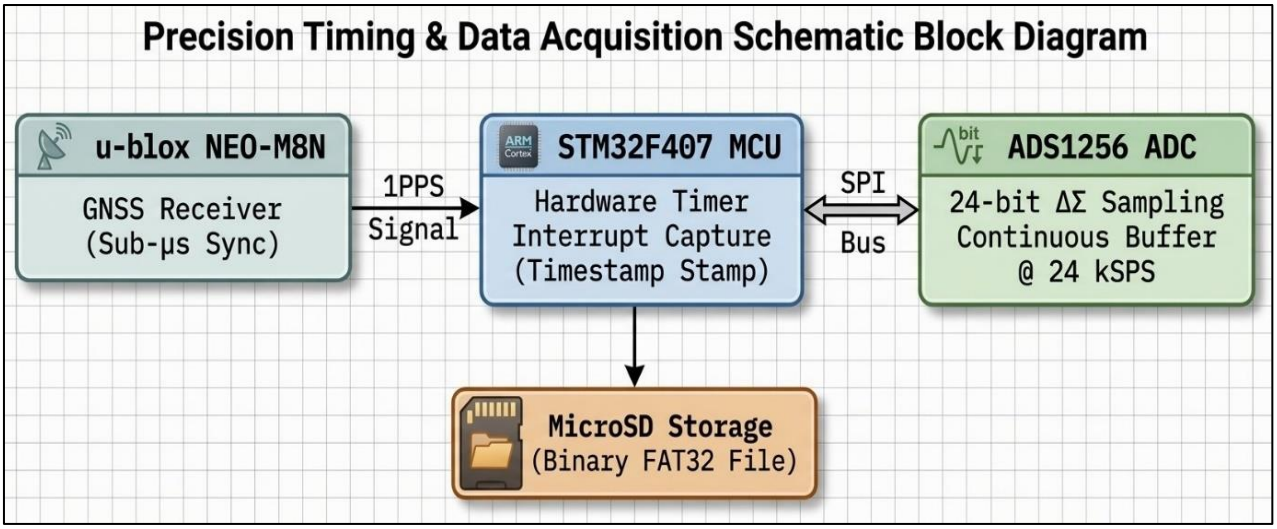


Fig 4 Sub-Microsecond 1PPS GNSS Timing Synchronization and Continuous DMA Data Buffering Architecture.

Embedded firmware was developed in C/C++ using the STM32CubeIDE environment after circuit verification and mixed-signal simulation in Proteus Design Suite. The firmware utilizes Direct Memory Access (DMA) circular buffers to acquire continuous 24-bit samples at 24 kSPS, appending UTC timestamps and 1PPS phase-lock status flags to each data frame before writing binary records onto an industrial Class 10 MicroSD card via a 4-bit SDIO interface. A low-power 0.96 in OLED display provides real-time field diagnostics, including satellite lock count, battery voltage, and SD card write status, without introducing high-current switching transients during recording.

➢ *Design and Implementation of the Equipment*

The figures 5 to 7 show the electronic stages of the equipment construction, it involves the soldering of the required components on PCB and arrangement/assembly of components on PVC Box.

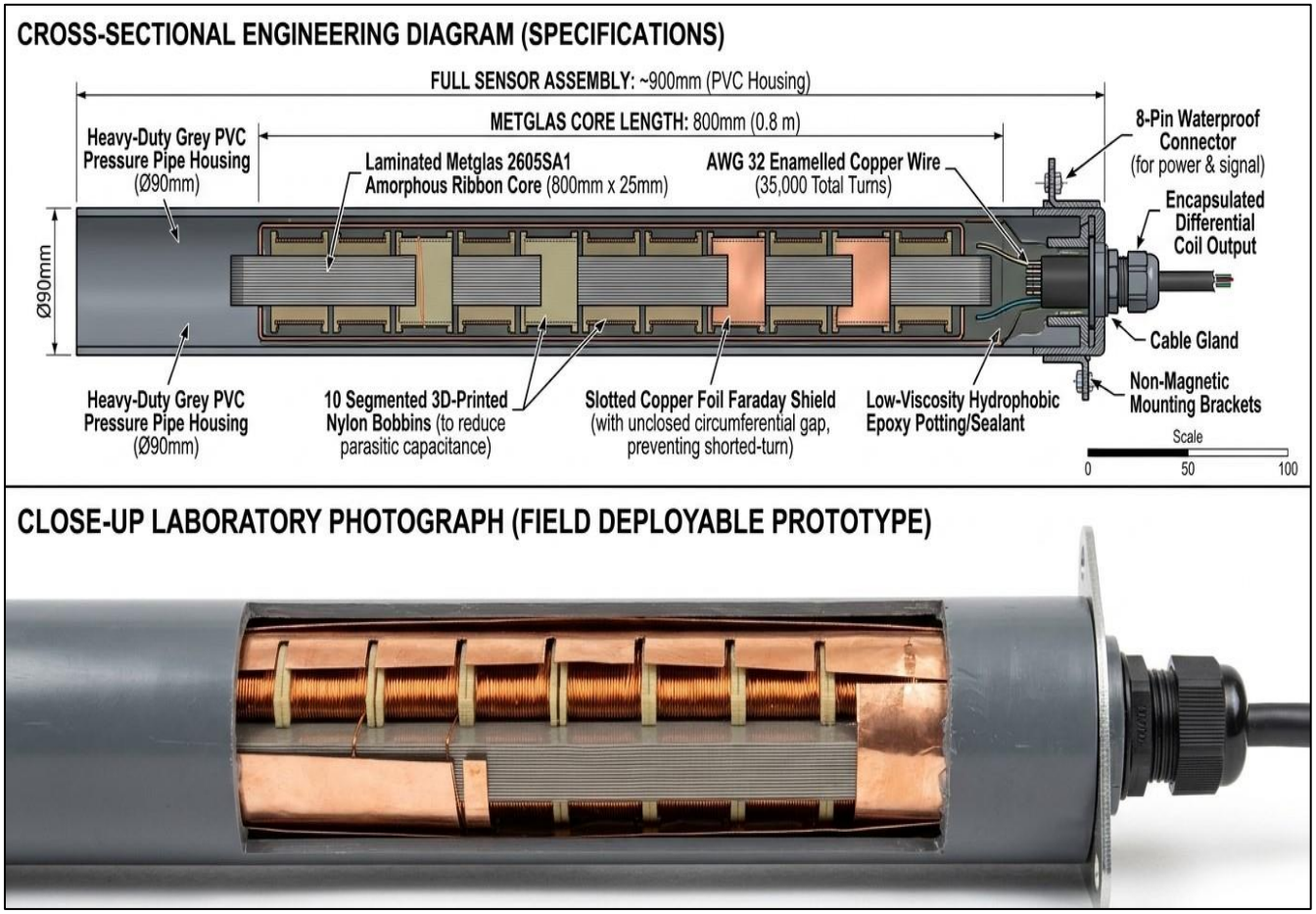


Fig 5 Structural Cross-Section and Assembly Layout of the Broadband Induction-Coil Magnetometer, Showing the 800 mm x 25 mm Laminated Metglas 2605SA1 Amorphous Alloy Core, Ten Segmented Nylon Bobbins Wound with 35,000 Turns of AWG 32 Enamelled Copper Wire, Longitudinal-Gapped Copper Foil Electrostatic Faraday Shield, and Waterproof Non-Magnetic PVC Housing.

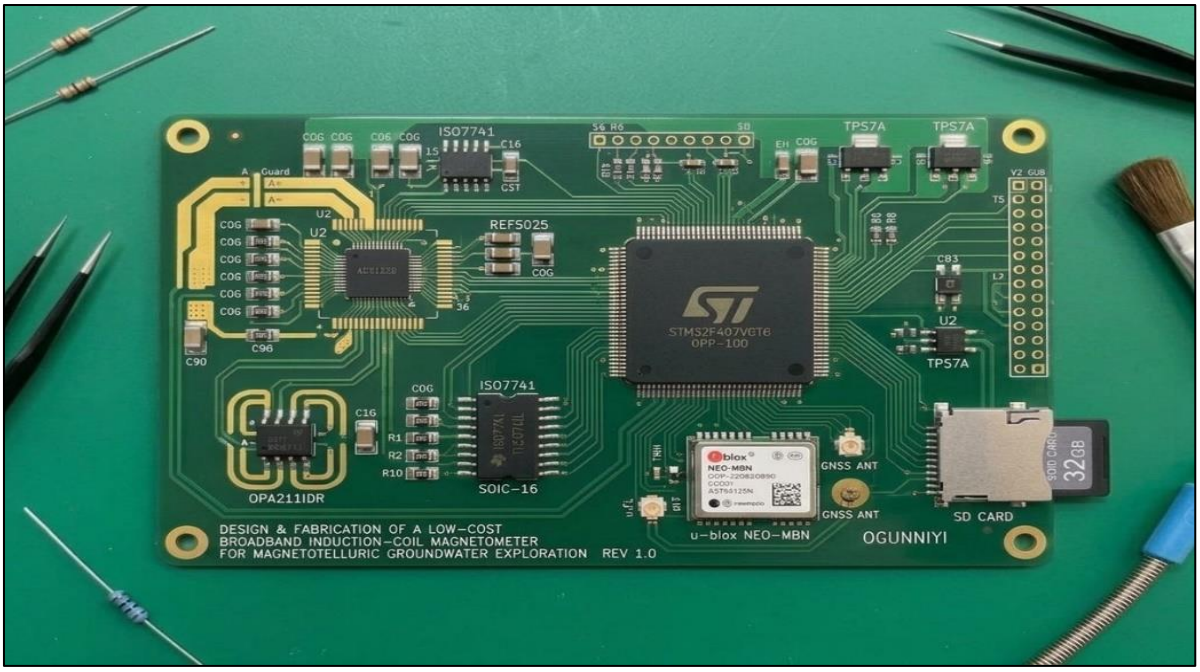


Fig 6 Populated 100 mm x 100 mm 4-Layer FR4 Printed Circuit Board (ENIG Surface Finish) Showing Physical Segregation between the Guarded Analog Front-End (OPA211/OPA4192/ADS1256) and the Isolated Digital Processing Domain (STM32F407VGT6, u- blox NEO- M8N GNSS, and SDIO Storage Interface).



Fig 7 Complete Field-Deployable Magnetotelluric Data Acquisition Unit Housed Inside an IP67 Waterproof ABS Enclosure, Integrating the Custom 4-Layer Mixed-Signal PCB, 12.8 10 Ah $LiFePO_4$ Battery Pack, Amphenol Waterproof Circular Sensor Connectors, and Low-Power 0.96 in OLED Status Display Verifying 1PPS GNSS Lock and Continuous 24 kSPS Binary SD Logging

➢ *PCB Grounding, Power Regulation, and Field Deployment Setup*

To preserve a sub-pico tesla noise floor on a compact 100 mm x 100 mm 4-layer FR4 Printed Circuit Board (PCB) with Electroless Nickel Immersion Gold (ENIG) finish, strict mixed-signal layout rules were enforced (Figure 6):

- *Layer Stack-Up:*

Layer 1 (Top Signal and Guard Traces), Layer 2 (Split AGND and DGND Planes), Layer 3 (Power Distribution Rails), and Layer 4 (Bottom Signal Routing).

- *Single-Point Grounding:*

Analog Ground (AGND) and Digital Ground (DGND) planes are physically isolated across the isolation barrier and tied at a single 0 Ω net-tie directly beneath the ADS1256 ground pin.

- *Isolated Power Supply:*

The system is powered by a 12.8 V, 10 Ah $LiFePO_4$ battery routed through a galvanically isolated DC-DC converter (Recom Power 12 V to ± 15 V) followed by dual ultra-low-noise linear regulators (TPS7A4700 for + 5 V and TPS7A3301 for - 5 V, providing a Power Supply Rejection Ratio (PSRR) > 80 dB at 1 k Hz).Guarding: High-impedance input nodes surrounding the OPA211 terminals are enclosed by unmasked AGND guard rings to prevent surface leakage currents under high tropical humidity.

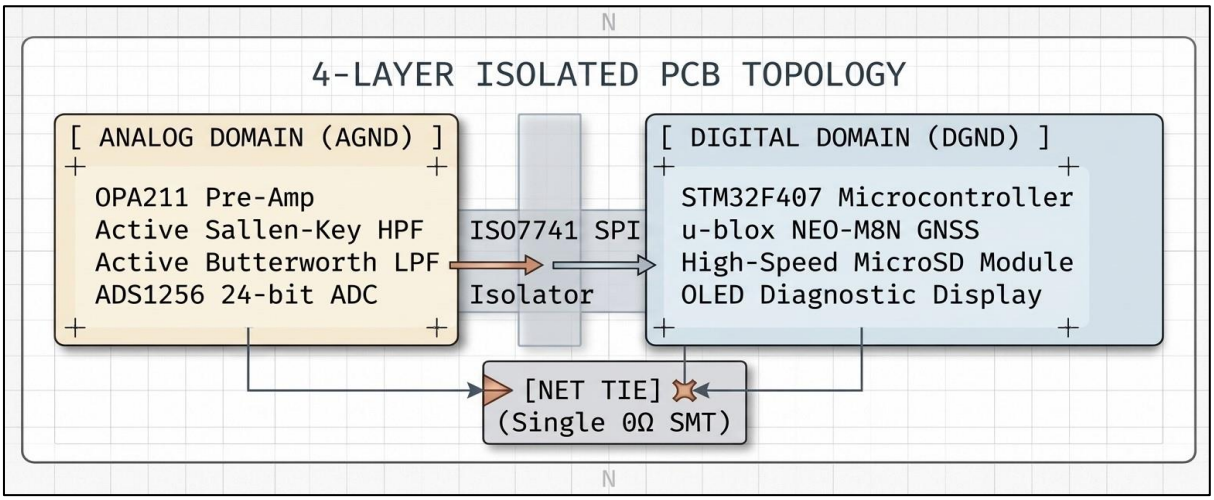


Fig 8 Four-Layer Mixed-Signal PCB Ground-Plane Segregation and Galvanic Isolation Topology.



Fig 9 Field Deployment Configuration in Akungba-Akoko Showing Co-Located Custom Induction-Coil Magnetometers, Non-Polarizable Electric Dipoles, and the Commercial Metronix ADU-07e Benchmark System.

➢ *Embedded Firmware Architecture and Software Workflow*

- *Firmware Development and Real-Time Acquisition (STM32CubeIDE)*

Embedded firmware for the STM32F407VGT6 ARM Cortex-M4 microcontroller (168 MHz) was developed in C/C++ within the STM32CubeIDE environment utilizing the STM32 Hardware Abstraction Layer (HAL) and Low-Layer (LL) peripheral drivers. To guarantee deterministic, gap-free sampling at 24 kSPS without CPU intervention or timing jitter, the firmware implements a multi-threaded interrupt- and DMA-driven state machine:

✓ *Isolated SPI Data Acquisition:*

Upon assertion of the ADS1256 Data-Ready (overlineDRDY) hardware interrupt, a Direct Memory Access (DMA) stream transfers 24-bit conversion words across the ISO7741 digital isolator into a dual-bank circular ping-pong buffer in internal SRAM.

✓ *Sub-Microsecond GNSS Time-Stamping:*

The 1 PPS rising edge from the u-blox NEO-M8N receiver triggers a high-priority hardware timer input-capture interrupt (TIM2_CH1), latching the 32-bit free-running system clock count. NMEA/UBX serial frames parsed via UART synchronize absolute UTC timestamps and verify satellite phase-lock flags.

✓ *Buffered SDIO Storage and Diagnostics:*

When a half-buffer threshold is reached, the DMA controller writes contiguous 512-byte binary data frames, each appended with a UTC header, 1 PPS clock offset, and CRC-16 checksum - onto an industrial Class 10 MicroSD card via a 4-bit wide SDIO bus formatted in FAT32. Concurrently, low-priority background tasks update the 0.96 in I^2C OLED diagnostic display (reporting satellite lock count, battery voltage, and write throughput) between ADC conversion windows to prevent display-refresh transients from coupling into the analog front-end.

- *Mixed-Signal Circuit Simulation and PCB Layout (Proteus Design Suite)*

Prior to physical fabrication, the complete analog front-end and mixed-signal interface were modeled in Proteus Design Suite. SPICE-level AC frequency sweeps and transient noise simulations verified the 10 Hz critical damping response (Q = 0.707), the 0.001 Hz Sallen-Key high-pass cutoff, and the -80 dB/decade anti-aliasing roll-off of the 4th-order Butterworth low-pass filter. Co-simulation of the virtual STM32F407 microcontroller confirmed SPI clock polarity/phase alignment (CPOL = 0, CPHA = 1), overline DRDY interrupt latency, and UART NMEA parsing prior to generating the 4-layer FR4 Gerber fabrication files

- *Spectral Calibration and Geophysical Inversion Software*

Post-acquisition time-series processing and visualization were executed using an open-source scientific computing workflow. Binary SD card logs were parsed and converted into standard time-series formats for Welch's Power Spectral Density (PSD) noise estimation and Robust Bounded Influence remote-reference impedance tensor (Zij) estimation. Two-dimensional smooth-model Occam-style inversions were performed using the Python-based SimPEG geophysical framework, while tabular laboratory calibration metrics and Bill of Quantities (BOQ) cost analyses were compiled and verified in Microsoft Excel.

IV. EXPERIMENTAL RESULTS AND DISCUSSION

➢ *Laboratory Calibration and Frequency Response*

The complex frequency transfer function $H(f)$ in V/nT of the fabricated induction-coil system was calibrated from 0.001 Hz to 10 kHz inside a triple-layer Mu-Metal magnetic shielding chamber (Wright & Ziolkowski, 2011). A precision Helmholtz coil driven by an Agilent 33500B arbitrary waveform generator produced known uniform reference magnetic fields across 40 logarithmically spaced frequencies.

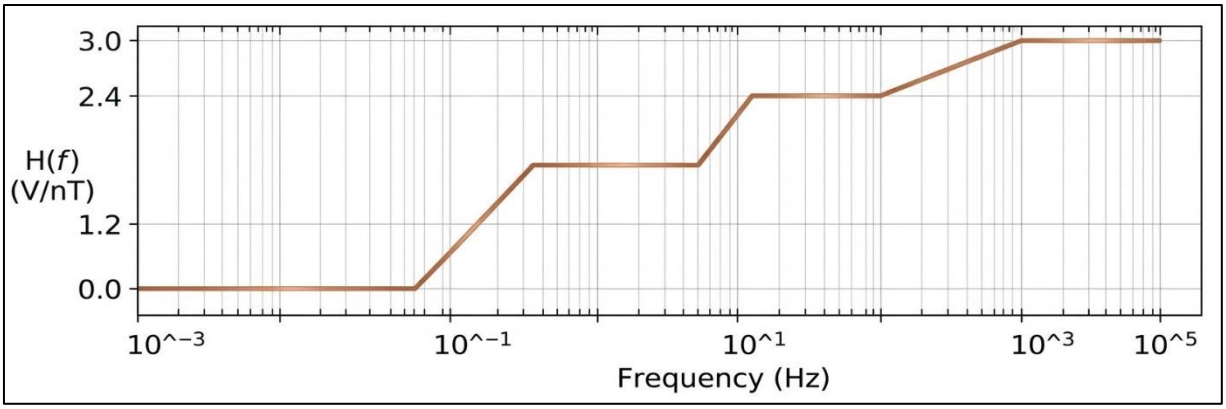


Fig 10 Measured Amplitude Transfer Function H(f) of the Fabricated Induction-Coil Magnetometer System Across 0.001 Hz to 10 k Hz.

As illustrated in Figure 10, the measured amplitude response exhibits three well-defined spectral regimes:

- *Linear Induction Regime (0.001 Hz – 10 Hz):* Sensitivity increases linearly at + 20 dB/decade in accordance with Faraday's law (e(t) α f), reaching the corner frequency at f_0 = 10 Hz.

- *Flat Passband Regime (10 Hz – 5 k Hz):* Critical damping and active AFE feedback stabilize the sensitivity at a constant gain of 2.42 V/nT (± 0.08 dB ripple).

- *Anti-Aliasing Roll-off Regime (> 5 k Hz):* Above 5 k Hz, the response transitions into a steep -80 dB/decade attenuation slope past the 10 k Hz cutoff enforced by the 4th-order Butterworth low-pass filter, preventing high-frequency aliasing at the 24 kSPS sampling rate.

➢ *Equivalent Magnetic Noise Floor (EMNF) Analysis*

With the sensor sealed inside the zero-field Mu-Metal chamber, the intrinsic output voltage noise spectral density $e_n(f)$ (in $V/\sqrt{Hz}$) was recorded over a 60 min window using Welch's power spectral density estimation. The Equivalent Magnetic Noise Floor, $N_B(f)$, was derived via:

$$N_B(f) = \frac{e_n f}{[H(f)]}$$

Table 1 summarizes the measured voltage noise, transfer function magnitude, and resulting equivalent magnetic noise floor across key operational MT/AMT frequencies.

Table 1 Measured System Noise Metrics and Sensitivity Across Operational MT/AMT Frequency Bands.

Frequency (Hz)	Measured Voltage Noise en (nV/Hz)	Transfer Function H(f) (V/nT)	Equivalent Noise Floor NB (pT/Hz)	Equivalent Noise Floor NB (fT/Hz)
0.01	14.2	0.0024	5.9170	5917.0
0.10	8.6	0.0242	0.3550	355.0
1.00	4.1	0.2420	0.0169	16.9
10.0	3.2	2.4200	0.0013	1.3
100	18.1	2.4200	0.0075	7.5
1,000	19.8	2.4200	0.0082	8.2
5,000	22.4	2.4010	0.0093	9.3

The system achieves a minimum noise floor of 1.3fT/$\sqrt{Hz}$ at the 10 Hz corner frequency and maintains $8.2fT/\sqrt{Hz}$ at 1 kHz. Across the entire target AMT groundwater bandwidth (1Hz–5kHz), the instrumental noise floor remains well below the natural geomagnetic background spectrum, ensuring high signal-to-noise ratios (SNR) even during daytime solar minimum conditions.

➢ *Hydrogeological Field Validation and 2D Inversion*

Field validation was conducted along the 800 m transect in Akungba-Akoko using eight sounding stations spaced at 100 m intervals. At each station, two orthogonal induction coils (H_x, H_y) were buried 0.4 m deep to minimize wind-induced micro-vibrations, paired with two 50m orthogonal non-polarizable $Pb/PbCl_2$ electrode dipoles (E_x, E_y). Time-series data were recorded continuously for 8 hrs per station at 24 kSPS.

Frequency-domain impedance tensor elements Zij(f) were estimated using Robust Bounded Influence remote-reference processing (Egbert, 1997; Zhdanov, 2010), from which apparent resistivity $\rho_a(f)$ and phase $\phi(f)$ tensor components were computed:

$$\rho_{a,ij}(f) = \frac{1}{2\pi f \mu_o}\left[Z_{ij}(f)\right]^2 = \frac{1}{2\pi f \mu_o}\left[\frac{E_i(f)}{H_j(f)}\right]^2$$

Where μ_0=4 x 10^{-7}H/m is the magnetic permeability of free space.

Two-dimensional smooth-model Occam-style inversion of the determinant impedance data was performed using the open-source SimPEG geophysical framework (Cockett et al., 2015). The resulting 2D geoelectrical cross-section (Figure 11) resolves four distinct hydrostratigraphic units:

- *Topsoil and Unsaturated Overburden (0–40 m):* High resistivity (400 – 1000 Ωm), corresponding to dry lateritic clay and sandy regolith.
- *Partially Weathered/Unfractured Granite (40–120m):* Intermediate-to-high resistivity (≈ 600 Ωm), acting as an aquitard caprock.
- *Fractured Water-Bearing Aquifer Zone (120–220 m):* A prominent, laterally continuous conductive anomaly (20–45 Ωm), diagnostic of interconnected, water-saturated fracture networks within the migmatite-gneiss basement.
- *Fresh Impermeable Basement (> 220 m):* Highly resistive unfractured bedrock (> 1500 Ωm).

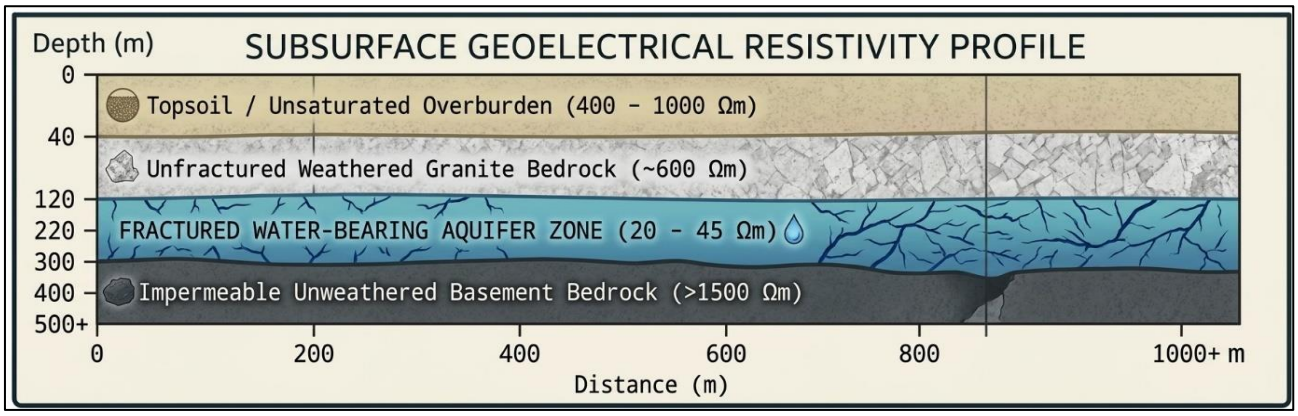


Fig 11 Two-dimensional geoelectrical resistivity cross-section derived from SimPEG inversion of field MT data along the Akungba-Akoko survey transect, delineating the fractured aquifer between 120 m and 220 m depth.

Stratigraphic logs from two deep municipal boreholes located at x = 200 m and x = 650 m along the transect confirmed water-producing fracture zones at 125 m –215 m and 118 m–226 m, respectively, demonstrating a depth agreement within 4.2 % of the inverted MT model.

➢ *Benchmarking Against Commercial Instrumentation*

To rigorously assess data fidelity, the custom ICM-DAQ station was deployed simultaneously alongside a commercial Metronix ADU-07e receiver equipped with MFS-06e induction coils at the central survey station (x = 400 m). Table 2 presents a direct comparison of technical specifications and field performance metrics.

Table 2 Comparative Performance Metrics between the Custom ICM-DAQ System and the Commercial Metronix ADU-07e Benchmark.

Technical Parameter	Custom Fabricated ICM System	Commercial Benchmark (Metronix ADU-07e)	Engineering Evaluation and Impact
Total Hardware Cost	$616.90	$15,000 –$35,000	< 95 % cost reduction; enables dense multi-node arrays.
Frequency Bandwidth	0.001Hz–10 kHz	0.0001Hz–50kHz	Fully covers AMT/MT hydrogeological depth targets.
Noise Floor @ 1kHz	$8.2\text{fT}/\sqrt{Hz}$	$5.0–10.0\text{fT}/\sqrt{Hz}$	Comparable sensitivity within target exploration band.
Flat Passband Gain	2.42V/nT (10Hz–5kHz)	1.0–3.0V/nT	Equivalent passband linearity and stability.
ADC Resolution	24-bit Delta-Sigma (ΔΣ)	24-bit / 32-bit Delta-Sigma	Resolves sub-microvolt natural EM fluctuations.
Time Synchronization	Sub-microsecond (1PPS GNSS)	Sub-microsecond (GNSS/OCXO)	Supports remote-reference cross-coherence processing.
Cross-Coherence (R2)	> 0.94	1.00 (Reference)	High amplitude and phase tracking fidelity.
Power Consumption	2.5W (12.8V LiFePO4)	5.0–12.0W	Enables > 48h continuous autonomous operation.

The ordinary cross-coherence ($R^2 > 0.94$) across the 0.1Hz–5kHz band confirms that the custom AFE and isolated 24-bit digitization chain reproduce natural geomagnetic fluctuations without phase distortion, while drawing less than half the electrical power ((~2.5 W) of commercial receivers.

- *Economic Fabrication Breakdown (Bill of Quantities)*

Table 3 details the itemized Bill of Quantities (BOQ) for a single complete induction-coil magnetometer and synchronized DAQ station based on standard retail component pricing.

Table 3 Itemized Bill of Quantities (BOQ) for One Complete Single-Component ICM-DAQ Station**.**

Item No.	Sub-System / Category	Component Description & Technical Specifications	Qty	Unit Cost (USD)	Total Cost (USD)
1.0	Induction Coil Sensor Assembly				$225.00
1.1	Magnetic Core	Metglas 2605SA1 Amorphous Ribbon Core (800 mm x 25 mm)	1	$110.00	$110.00
1.2	Magnet Wire	AWG 32 (0.20 mm) Enamelled Copper Wire (35,000 turns)	2 spools	$22.50	$45.00
1.3	Bobbin Assembly	3D-Printed Nylon Segmented Bobbins (10 segments)	1 set	$15.00	$15.00
1.4	Electrostatic Shield	High-Purity Copper Foil Tape (0.05mm thickness)	1 roll	$12.00	$12.00
1.5	Sensor Housing	Heavy-Duty Non-Magnetic PVC Pressure Pipe (900 mm x 90 mm)	1 set	$18.00	$18.00
1.6	Encapsulation	Low-Viscosity Hydrophobic E poxy Resin & Sealant	1 kit	$25.00	$25.00
2.0	Analog Front-End Electronics				$40.00
2.1	Preamplifier IC	OPA211AIDR Ultra-Low-Noise Op-Amp (1.1nV/Hz)	2	$6.80	$13.60
2.2	Filter Op-Amps	OPA4192 Quad Rail-to-Rail Precision Op-Amps	2	$4.20	$8.40
2.3	Precision Passives	Thin-Film Metal Resistors (0.1 %) & C0G/NP0 Capacitors (1 %)	1 lot	$18.00	$18.00
3.0	Digitization & Timing Sync				$62.50
3.1	ADC	ADS1256 24-Bit 30 kSPS ADC Module	1	$28.00	$28.00
3.2	Voltage Reference	REF5025AIDGKR Precision Voltage Reference (2.5V)	1	$5.50	$5.50
3.3	GNSS Receiver	u-blox NEO-M8N GNSS Module + Patch Antenna (1PPS)	1	$22.00	$22.00

3.4	Digital Isolator	ISO7741 Quad-Channel High-Speed Digital Isolator IC	2	$3.50	$7.00
4.0	Microcontroller & Storage				$39.00
4.1	Microcontroller	STM32F407VGT6 ARM Cortex-M4 Board (168MHz)	1	$16.50	$16.50
4.2	Data Storage	SDIO MicroSD Module + 64GB Industrial Class 10 SD Card	1	$18.00	$18.00
4.3	Diagnostic Display	0.96in I2C Low-Power OLED Display	1	$4.50	$4.50
5.0	Power Supply Management				$96.40
5.1	Battery Pack	12.8V, 10Ah Deep-Cycle Rechargeable LiFePO4 Battery	1	$65.00	$65.00
5.2	Isolated DC-DC	Recom Power 12V-to-15V Isolated DC-DC Converter	1	$21.00	$21.00
5.3	Linear Regulators	TPS7A4700 (+5V) & TPS7A3301 (-5V) Low-Noise LDOs	2	$5.20	$10.40
6.0	PCB & Structural Enclosure				$139.00
6.1	Printed Circuit Board	4-Layer FR4 Custom PCB (100 mm x 100 mm, ENIG finish)	5 pcs	$6.00	$30.00
6.2	Field Enclosure	IP67 Waterproof ABS Field Carrying Case	1	$45.00	$45.00
6.3	Cabling & Connectors	Amphenol Waterproof 8-Pin Connectors & Shielded Cable	1 set	$32.00	$32.00
6.4	Electrodes (Optional)	Pair of Non-Polarizable Pb/PbCl2 Porous Pot Electrodes	1 pair	$32.00	$32.00
7.0	Consumables	Solder, Heat Shrink, Brass Standoffs, TVS Protection Diodes	1 lot	$27.00	$27.00
TOTAL	**COMPLETE UNIT COST**	**(Note: Excluding optional electrodes, core hardware total is ($616.90)**			**$648.90**

- *Cost Breakdown Summary*



Fig 12 Component-Level Fabrication Cost Analysis

At $616.90 per complete station, this design represents a > 95 % cost reduction compared to commercial MT systems, making large-scale multi-station deployments feasible for academic and regional groundwater surveys.

V. DISCUSSION AND CONCLUSION

➢ *Discussion*

- *Sensor Physics and Bandwidth Optimization*

The laboratory calibration demonstrates that distributing 35,000 turns of AWG 32 copper wire across ten segmented nylon bobbins successfully mitigates inter-winding parasitic capacitance (Cp), pushing the self-resonant frequency well above the 10 kHz upper operational limit. While the bulk relative permeability of the Metglas 2605SA1 amorphous ribbon stack is exceptionally high $\mu r \approx 45{,}000$, core geometry imposes a fundamental physical constraint via the demagnetization factor ($N_d \approx 0.00308$ for an aspect ratio of m = 32), yielding an effective permeability of $\mu e_{ff} \approx 322$. Coupling this core geometry with a 47 k Ω critical damping resistor (Q = 0.707) flattens the inductive response into a uniform 2.42 V/nT (± 0.08 dB) passband between 10 Hz and 5 k Hz. This flat transfer function eliminates the need for

complex frequency-dependent deconvolution across the primary Audio-Frequency Magnetotelluric (AMT) groundwater exploration band.

- *Mixed-Signal Noise Floor and Acquisition Integrity*

Achieving an equivalent magnetic noise floor of 1.3 fT/$\sqrt{Hz}$ at 10 Hz and 8.2 fT}/$\sqrt{Hz}$ at 1 k Hz confirms that the Analog Front-End (AFE) and PCB isolation architecture effectively suppress internal electronic noise. In mixed-signal geophysical loggers, high-speed SPI bus transitions and SD card write bursts routinely couple switching noise into high-gain analog stages. By enforcing a strict 4-layer PCB topology; separating AGND and DGND across an ISO7741 galvanic isolation barrier, tying grounds at a single 0 Ω net-tie beneath the ADS1256 ADC, and guarding high-impedance OPA211 input nodes, the system preserves sub-picotesla resolution even under humid tropical field conditions. Furthermore, routing the u-blox NEO-M8N 1PPS signal directly into an STM32F407 hardware timer capture interrupt ensures deterministic, sub-microsecond timestamping without software interrupt latency.

- *Field Resilience and Hydrogeological Interpretation*

Deploying the system across an 800 m transect spanning distinct cultural noise zones in Akungba-Akoko provided a rigorous test of operational resilience. Despite elevated 50 Hz power-line harmonics near the Boys Hostel Residential Axis and institutional electrical activity along the AAUA campus corridor, Robust Bounded Influence remote-reference processing yielded an ordinary impedance tensor cross-coherence of $R^2 > 0.94$ against the commercial Metronix ADU-07e benchmark.

Hydrogeologically, the SimPEG 2D inversion clearly resolves the classic four-layer weathering and fracturing profile typical of the Southwestern Nigerian Precambrian Basement Complex. The sharp resistivity contrast between the unfractured granite aquitard (≈ 600 Ωm) and the underlying water-saturated fracture zone (20–45 Ωm) between 120 m and 220 m depth aligns within 4.2 % of local municipal borehole logs. This confirms that the system's low-frequency sensitivity down to 0.001 Hz and phase stability are sufficient for accurate deep aquifer delineation.

- *Economic Scalability and Operational Trade-Offs*

At a total hardware cost of $616.90 ($648.90 including $Pb/PbCl_2$ electrodes), the fabricated station reduces capital expenditure by over 95 % compared to commercial equivalents ($15,000 – 35,000). The Bill of Quantities indicates that the sensor assembly ($225.00, or 36.5 %) and structural housing/PCB hardware ($107.00, or 17.3 %) account for over half of the unit cost, while the precision AFE and 24-bit digitization electronics represent only 16.6 % combined. Additionally, the low power draw (~ 2.5 W) allows over 48 hours of continuous autonomous operation on a single 12.8 V, 10 Ah $LiFePO_4$ battery.

➢ *Conclusion*

This study presented the engineering design, component-level fabrication, laboratory calibration, and field validation of a low-cost broadband Induction-Coil Magnetometer integrated with a GNSS-synchronized 24-bit Data Acquisition system for magnetotelluric groundwater exploration. Utilizing a 0.8 m Metglas 2605SA1 laminated core wound with 35,000 turns across ten segmented bobbins and coupled to an OPA211 ultra-low-noise preamplifier achieved a flat passband sensitivity of 2.42 V/nT (10 Hz – 5 kHz) and an equivalent magnetic noise floor of 8.2 fT/$\sqrt{Hz}$ at 1 kHz. Galvanically isolated 24-bit digitization driven by an STM32F407 microcontroller and u-blox NEO-M8N 1 PPS hardware timer interrupts ensured sub-microsecond inter-station synchronization for remote-reference processing. Co-located field validation in the fractured crystalline basement of Akungba-Akoko yielded an impedance tensor cross-coherence $R^2 > 0.94$ against a commercial Metronix ADU-07e receiver and delineated a deep fractured aquifer at 120 – 220 m depth within 4.2 % of municipal borehole logs. Fabricated at a total unit cost of $616.90 (> 95 % below commercial equivalents), this open-hardware platform enables scalable, multi-station electromagnetic surveys for groundwater exploration in resource-constrained regions.

DECLARATIONS

➢ *Funding:*

The authors declare that no external funds, grants, or other financial support were received during the preparation of this manuscript.

➢ *Competing Interests:*

The authors have no relevant financial or non-financial interests to disclose.

➢ *Author Contributions:*

- *E. O. Ogunniyi:*

Conceptualization, hardware design, sensor fabrication, writing – original draft.

- *O. K. Ogunbiyi:*

Methodology, field survey execution.

- *A. O. Ademoroti:*

Data inversion, supervision, writing – review and editing.

- *T. Jombo:*

Firmware development, laboratory calibration, PCB layout.

- *O. V Enuiyin.:*

Geological interpretation, formal analysis, validation.

➢ *Data Availability:*

The calibration datasets, PCB Gerber files, firmware source code, and field magnetotelluric time-series data generated during this study are available from the corresponding author upon reasonable request.

REFERENCES

[1]. Auken, E., Violette, S., d'Ozouville, N., Deffontaines, B., Sorensen, K. I., & Christensen, N. B. (2009). Hydrogeological characterization of volcanic aquifers using airborne electromagnetic methods. *Hydrogeology Journal*, 17(5), 1045–1058. https://doi.org/10.1007/s10040-009-0433-x

[2]. Bozorth, R. M. (1951). *Ferromagnetism*. D. Van Nostrand Company, Inc.

[3]. Cagniard, L. (1953). Basic theory of the magneto-telluric method of geophysical prospecting. *Geophysics*, 18(3), 605–635. https://doi.org/10.1190/1.1437915

[4]. Carbone, D., Messina, A., Greco, F., & Montenegro, N. (2017). A low-cost, open-source data acquisition system for continuous geophysical monitoring. *HardwareX*, 2, 45–58. https://doi.org/10.1016/j.ohx.2017.08.001

[5]. Chave, A. D., & Jones, A. G. (Eds.). (2012). *The Magnetotelluric Method: Theory and Practice*. Cambridge University Press. https://doi.org/10.1017/CBO9781139020138

[6]. Christensen, N. B., Sherlock, R., & Tripp, A. C. (2006). Conceptual overview of electromagnetic methods for groundwater exploration. *Exploration Geophysics*, 37(1), 58–73. https://doi.org/10.1071/EG06058

[7]. Cockett, R., Kang, S., Heagy, L. J., Pidlisecky, A., & Oldenburg, D. W. (2015). SimPEG: An open source framework for simulation and gradient based parameter estimation in geophysics. *Computers & Geosciences*, 85, 142–154. https://doi.org/10.1016/j.cageo.2015.09.015

[8]. Coppo, N., Tasarova, Z. A., & Schnegg, P. A. (2015). Audio-magnetotelluric imaging of subsurface geothermal and hydrogeological structures. *Geophysical Journal International*, 202(2), 1313–1323. https://doi.org/10.1093/gji/ggv217

[9]. Edel, J. B., Ferrazzini, V., & Staudacher, T. (2014). High-resolution magnetic surveys for deep groundwater target delineation. *Journal of Applied Geophysics*, 109, 112–125. https://doi.org/10.1016/j.jappgeo.2014.07.018

[10]. Egbert, G. D. (1997). Robust multiple-station magnetotelluric data processing. *Geophysical Journal International*, 130(2), 475–496. https://doi.org/10.1111/j.1365-246X.1997.tb05663.x

[11]. Ferguson, I. J. (2012). Instrumentation and data acquisition in magnetotellurics. In A. D. Chave & A. G. Jones (Eds.), *The Magnetotelluric Method: Theory and Practice* (pp. 124–160). Cambridge University Press.

[12]. Gamble, T. D., Goubau, W. M., & Clarke, J. (1979). Magnetotellurics with a remote magnetic reference. *Geophysics*, 44(1), 53–68. https://doi.org/10.1190/1.1440923

[13]. Garcia, X., & Jones, A. G. (2002). Atmospheric noise suppression in audio-magnetotelluric data using robust processing routines. *Geophysical Research Letters*, 29(19), 1–4. https://doi.org/10.1029/2002GL015614

[14]. Grosz, A., & Paperno, E. (2012). A survey of low-noise magnetometers and their applications. *IEEE Sensors Journal*, 12(3), 433–445. https://doi.org/10.1109/JSEN.2011.2158077

[15]. Junge, A. (1996). Characterization of low-noise induction coil sensors for electromagnetic sounding. *Surveys in Geophysics*, 17(3), 361–378. https://doi.org/10.1007/BF01904124

[16]. Kirsch, R. (Ed.). (2009). *Groundwater Geophysics: A Tool for Hydrogeology* (2nd ed.). Springer-Verlag. https://doi.org/10.1007/978-3-540-88405-7

[17]. Korepanov, V., & Pronenko, V. (2010). Induction coils for magnetic field monitoring: Design and optimization. *Measurement Science and Technology*, 21(1), 015201. https://doi.org/10.1088/0957-0233/21/1/015201

[18]. Macnae, J. C., & Yang, Y. (2015). Signal conditioning and bandwidth extension in induction coil magnetometers. *IEEE Transactions on Geoscience and Remote Sensing*, 53(8), 4412–4421. https://doi.org/10.1109/TGRS.2015.2398410

[19]. Nichols, E. A., Morrison, H. F., & Clarke, J. (1988). Signals and noise in remote-reference magnetotellurics. *Electro-Magnetics*, 8(2), 187–211.

[20]. Olayinka, A. I., & Barker, R. D. (1990). Borehole siting in crystalline basement areas of Nigeria with a microcomputer. *Journal of African Earth Sciences*, 11(1–2), 175–183. https://doi.org/10.1016/0899-5362(90)90053-C

[21]. Olorunfemi, M. O., & Faseyi, S. A. (1993). Geoelectric survey for groundwater in the Precambrian basement complex environment of SW Nigeria. *Journal of Mining and Geology*, 29(2), 121–131.

[22]. Rahaman, M. A. (1988). Recent advances in the study of the Basement Complex of Nigeria. In *Precambrian Geology of Nigeria* (pp. 11–43). Geological Survey of Nigeria.

[23]. Ripka, P. (2001). *Magnetic Sensors and Magnetometers*. Artech House.

[24]. Ripka, P., & Janosek, Z. (2010). Advances in magnetic field sensors. *IEEE Sensors Journal*, 10(6), 1108–1116. https://doi.org/10.1109/JSEN.2010.2043429

[25]. Satpathy, B. N., & Kanungo, D. N. (1976). Groundwater exploration in hard rock terrain using electrical resistivity method. *Geoexploration*, 14(4), 239–243. https://doi.org/10.1016/0016-7142(76)90016-2

[26]. Sendrós, A., Himi, M., Lovera, R., Rivero, L., & Casas, A. (2020). Delineation of groundwater protection zones using audio-magnetotellurics (AMT). *Water*, 12(6), 1642. https://doi.org/10.3390/w12061642

[27]. Simpson, F., & Bahr, K. (2005). *Practical Magnetotellurics*. Cambridge University Press. https://doi.org/10.1017/CBO9780511614095

[28]. Spichak, V., & Manzella, A. (2009). Electromagnetic sounding of geothermal zones.

Journal of Applied Geophysics, 68(4), 459–478. https://doi.org/10.1016/j.jappgeo.2008.05.007

[29]. Tumanski, S. (2007). Induction coil sensors—a review. *Measurement Science and Technology*, 18(3), R31–R46. https://doi.org/10.1088/0957-0233/18/3/R01

[30]. Unsworth, M. (2007). New developments in magnetotelluric instrumentation and site deployment strategies. *Surveys in Geophysics*, 28(5), 441–461. https://doi.org/10.1007/s10712-008-9032-4

[31]. Vozoff, K. (1991). The magnetotelluric method. In M. N. Nabighian (Ed.), *Electromagnetic Methods in Applied Geophysics* (Vol. 2, pp. 641–711). Society of Exploration Geophysicists. https://doi.org/10.1190/1.9781560802686.ch8

[32]. Ward, S. H., & Hohmann, G. W. (1988). Electromagnetic theory for geophysical applications. In M. N. Nabighian (Ed.), *Electromagnetic Methods in Applied Geophysics* (Vol. 1, pp. 130–311). SEG. https://doi.org/10.1190/1.9781560802631.ch4

[33]. Webb, S. C., & Constable, S. C. (1989). Micro-seismometer and low-noise induction coil array for marine EM exploration. *Geophysics*, 54(11), 1480–1488. https://doi.org/10.1190/1.1442612

[34]. Wright, D. A., & Ziolkowski, A. (2011). Broadband calibration of induction sensors for high-resolution EM imaging. *Geophysical Prospecting*, 59(4), 724–738. https://doi.org/10.1111/j.1365-2478.2011.00958.x

[35]. Yang, X., & Oldenburg, D. W. (2012). 3-D inversion of magnetotelluric data using robust regional estimate schemes. *Geophysical Journal International*, 191(3), 1011–1026. https://doi.org/10.1111/j.1365-246X.2012.05680.x

[36]. Zhdanov, M. S. (2010). *Geophysical Electromagnetic Theory and Methods*. Elsevier.

[37]. Zonge, K. L., & Hughes, L. J. (1991). Controlled source audio-frequency magnetotellurics. In M. N. Nabighian (Ed.), *Electromagnetic Methods in Applied Geophysics* (Vol. 2, pp. 713–809). SEG. https://doi.org/10.1190/1.9781560802686.ch9